

# Automatic Detection of Regional Heart Rejection in USPIO-Enhanced MRI

Hsun-Hsien Chang, *Member, IEEE*, José M. F. Moura\*, *Fellow, IEEE*, Yijun L. Wu, and Chien Ho

**Abstract**—Contrast-enhanced magnetic resonance imaging (MRI) is useful to study the infiltration of cells *in vivo*. This research adopts ultrasmall superparamagnetic iron oxide (USPIO) particles as contrast agents. USPIO particles administered intravenously can be endocytosed by circulating immune cells, in particular, macrophages. Hence, macrophages are labeled with USPIO particles. When a transplanted heart undergoes rejection, immune cells will infiltrate the allograft. Imaged by  $T_2^*$ -weighted MRI, USPIO-labeled macrophages display dark pixel intensities. Detecting these labeled cells in the image facilitates the identification of acute heart rejection. This paper develops a classifier to detect the presence of USPIO-labeled macrophages in the myocardium in the framework of spectral graph theory. First, we describe a USPIO-enhanced heart image with a graph. Classification becomes equivalent to partitioning the graph into two disjoint subgraphs. We use the Cheeger constant of the graph as an objective functional to derive the classifier. We represent the classifier as a linear combination of basis functions given from the spectral analysis of the graph Laplacian. Minimization of the Cheeger constant based functional leads to the optimal classifier. Experimental results and comparisons with other methods suggest the feasibility of our approach to study the rejection of hearts imaged by USPIO-enhanced MRI.

**Index Terms**—Acute heart rejection, cardiac magnetic resonance imaging (MRI), Cheeger constant, classification, classifier, contrast agents, graph cut, graph Laplacian, spectral graph theory, ultrasmall superparamagnetic iron oxide (USPIO)-enhanced MRI.

## I. INTRODUCTION

**H**EART failure is a major public health crisis in the United States. It is the leading cause of death and hospitalization in this country. For many patients with end-stage heart failure, heart transplantation may be the only viable treatment option. Physicians typically assess for cardiac rejection by performing frequent endomyocardial biopsies. Using biopsy samples, cardiologists monitor immune cell infiltration and other pathological characteristics of rejection. However, biopsies are invasive procedures that are subject to patient risk. In addition, due to limited sampling, biopsies may not detect focal areas of rejection.

Manuscript received June 19, 2007; revised December 10, 2007. First published February 8, 2008; last published July 25, 2008 (projected). This work was supported by the National Institutes of Health under Grant P41EB001977 and Grant R01HL081349. *Asterisk indicates corresponding author.*

H. H. Chang is with Harvard Medical School, Boston, MA 02115 USA (e-mail: hsun-hsien.chang@childrens.harvard.edu).

\*J. M. F. Moura is with the Department of Electrical and Computer Engineering, Carnegie Mellon University, 5000 Forbes Ave., Pittsburgh, PA 15213 USA (e-mail: moura@ece.cmu.edu).

Y. L. Wu and C. Ho are with the Department of Biological Sciences and the Pittsburgh NMR Center for Biomedical Research, Carnegie Mellon University, Mellon Institute, Pittsburgh, PA 15213 USA.

Digital Object Identifier 10.1109/TMI.2008.918329

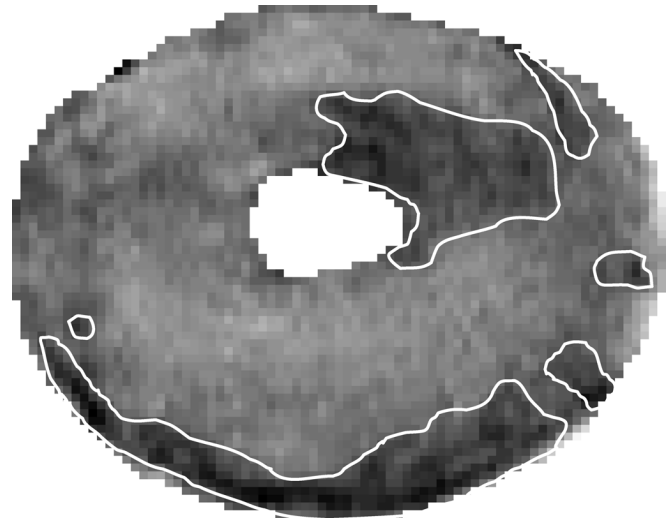


Fig. 1. USPIO-enhanced cardiac MR image where the dark pixels are segmented. Dark pixels correspond to the locations of USPIO-labeled abnormal cells.

Cellular magnetic resonance imaging (MRI) is a useful tool to noninvasively monitor the migration and localization of cells in the whole heart *in vivo* [1]. This imaging modality relies on extrinsic contrast agents, such as ultrasmall superparamagnetic iron oxide (USPIO) particles. The superior relaxivity of USPIO particles reduces signal emission in  $T_2^*$ -weighted MRI [2]. In other words, the signal attenuation created in  $T_2^*$ -weighted MR images localizes the cells containing a significant number of USPIO particles.

Mammalian cells can be labeled with MRI contrast agents either *ex vivo* or *in vivo*. In the *ex vivo* method, specific types of cells are isolated, labeled with contrast agents in culture, and then reintroduced. *In vivo* method, contrast agents are administered intravenously. In the *in vivo* labeling is effective for cells that can phagocytose or endocytose the contrast agents, and can be conveniently applied in the clinical studies. We adopt *in vivo* labeling in this study.

After USPIO particles are administered, circulating macrophages can endocytose USPIO particles and become USPIO-labeled macrophages. When rejection occurs, the labeled macrophages migrate to the rejecting tissue. Imaging the transplant by  $T_2^*$ -weighted MRI, dark pixels represent the infiltration of macrophages labeled by USPIO particles and identify the rejecting sites [3], [4]. For example, Fig. 1 shows the left ventricular image of a rejecting cardiac allograft, where the darker signal intensities in the myocardium reveal the presence of USPIO-labeled cells, leading to the detection of the

macrophage accumulation. To identify such regions, the first task is to classify the USPIO-labeled dark pixels in the image.

The usual method to classify USPIO-labeled pixels is manual classification [4]–[7], or simple thresholding of the image. Manual classification requires cardiologists to scrutinize the entire image to determine the location of the USPIO-labeled pixels. Manual classification is labor intensive and operator dependent. In addition, the noise introduced during the imaging, the blur induced by cardiac motion, and the partial volume effect make dark and bright pixels difficult to distinguish. Thresholding the intensities is the simplest algorithm to classify USPIO-labeled pixels; however, this method cannot handle noise. Another drawback of thresholding is that the operator has to adjust the threshold values, which may introduce inconsistent recordings. To reduce the labor involved with manual classification, to make the process robust to noise, and to achieve consistent results, we propose to develop an automatic algorithm for classification of USPIO-labeled pixels.

To design an automatic classification algorithm, we face the following challenges.

- 1) Macrophages accumulate in multiple regions without known pattern. For example, Fig. 1 displays a rejecting heart where the boundaries of macrophage accumulation are manually determined. We can see that the macrophage spread randomly throughout the myocardium. Since there is no model describing how macrophages infiltrate, the algorithm will rely solely on the MRI data.
- 2) Due to noise and cardiac motion, the boundaries between the dark and bright pixels are diffuse and hard to distinguish; as such, any classification algorithm has to be robust to noise.
- 3) There are a large number of pixels in the myocardium. For instance, the heart shown in Fig. 1 has more than 2500 myocardial pixels. This means that we have to classify more than 2500 pixels, which may involve estimating a large number of parameters. To avoid estimating too many parameters and design the classification algorithm in a tractable way, we transform the problem into another one that expresses the classifier in terms of a small number of parameters.
- 4) There are two types of classifiers for our design: supervised and unsupervised. Supervised classifiers need human operators to label a subset of the pixels. The classifiers then automatically propagate the human labels to the remaining pixels. However, the human knowledge might be unreliable, so the classification results are sensitive to operators. To avoid the classification inconsistency related to operator dependence, the classifier will be unsupervised.

#### A. Overview of Our Approach

We formulate the task of classifying USPIO-labeled regions as a problem of graph partitioning [8]. Given a heart image, the first step is to represent the myocardium as a graph. We treat all the myocardial pixels as the vertices of a graph, and prescribe a way to assign edges connecting the vertices. Graph partitioning is a method that separates the graph into disconnected subgraphs, for example, one representing the classified USPIO-labeled region and the other representing the unlabeled

region of the myocardium. The goal in graph partitioning is to find a small as possible subset of edges whose removal will separate out a large as possible subset of vertices. In graph theory terminology, the subset of edges that disjoins the graph is called a *cut*, and the measure to compare partitioned subsets of vertices is the *volume*. Graph partitioning finds the *minimal* ratio of the cut to the volume, which is called the *isoperimetric number* and is also known as the *Cheeger constant* [9] of the graph. Evaluating the Cheeger constant will determine the optimal edge cut.

The determination of the Cheeger constant, and hence of the optimal edge cut, is a combinatorial problem. We can enumerate all the possible combinations of two subgraphs partitioning the original graph, and then choose the combination with the smallest cut-to-volume ratio. However, when the number of vertices is very large, the enumeration approach is infeasible. To circumvent this obstacle, we adopt an optimization framework. We introduce a classifier, or a classification function, that determines to which class each pixel belongs, and derive from the Cheeger constant an objective functional to be minimized with respect to the classifier. The minimization leads to the optimal classification.

If there is a complete set of basis functions on the graph, we can represent the classifier by a linear combination of the basis. There are various ways to obtain the basis functions, e.g., using the Laplacian operator [10], the diffusion kernel [11], or the Hessian eigenmap [12]. Among these, we choose the Laplacian. The spectrum of the Laplacian operator has been used to obtain upper and lower bounds on the Cheeger constant [8]; we utilize these bounds to derive our objective functional. The eigenfunctions of the Laplacian form a basis of the Hilbert space of square integrable functions defined on the graph. Thus, we express the classifier as a linear combination of the Laplacian eigenfunctions. Since the basis is known, the optimal classifier is determined by the linear coefficients in the combination. The classifier can be further approximated as a linear combination of only the *most relevant* basis functions. The approximation reduces significantly the problem of looking for a large number of coefficients to estimating only a few of them. Once we determine the optimal coefficients, the optimal classifier automatically partitions the myocardial image into USPIO-labeled and unlabeled parts.

#### B. Paper Organization

This paper extends our work briefly presented in [13]. The organization of this paper is as follows. Section II describes how we represent a heart image by a graph and introduces the Cheeger constant for graph partitioning. Section III details the optimal classification algorithm in the framework of spectral graph theory. In Section IV, we describe the algorithm implementation and show our experimental results for USPIO-enhanced MRI data on heart transplants. We contrast the proposed method with the results of manual classification, thresholding, another graph based algorithm, and the level set approach. Finally, Section V concludes this paper.

## II. GRAPH REPRESENTATION AND GRAPH PARTITIONING

For a given USPIO-enhanced MR image, we first segment the left ventricle. Then, the myocardial pixels are arranged into a single column vector indexed by a set of integers

$I = \{1, 2, \dots, N_{\text{myo}}\}$ , where  $N_{\text{myo}}$  is the number of myocardial pixels. The image intensity becomes a function  $f : I \mapsto \mathbb{R}$ . We next describe how to represent the image as a graph.

**A. Weighted Graph Representation**

A graph  $G(V, E)$  has a set  $V$  of vertices and a set  $E$  of edges linking the vertices. For the segmented myocardium, we treat each myocardial pixel  $i$  as a vertex  $v_i$ . We next assign edges connecting the vertices. In the graph representation, the vertices with high possibility of being drawn from the same class are linked together. There are two strategies to assign edges.

- 1) Connect vertices to geographically neighboring vertices [14], because the neighborhood is usually drawn from the same class.
- 2) Connect vertices with similar features [10], because pixels in the same class generate the same features up to noise.

We adopt both strategies to build up our graph representation of the image.

With reference to Fig. 2(a), consider vertex  $v_i$  corresponding to pixel  $i$  at coordinate  $(x_i, y_i)$ . We connect  $v_i$  to its four neighboring vertices at coordinates  $(x_i + 1, y_i)$ ,  $(x_i - 1, y_i)$ ,  $(x_i, y_i + 1)$ , and  $(x_i, y_i - 1)$ . Fig. 2(a) illustrates the graph representation resulting from this rule of geographical neighborhood for a  $4 \times 4$  image. In this figure, each square is a pixel, and hence a vertex, and each line is an edge.

To account for strategy 2), we need features associated with the vertices and need a metric to determine the similarity between pairs of features. To take into account noise, we treat each pixel as a random variable and adopt the *Mahalanobis distance*, [15], as similarity measure. We stack a  $N_w \times N_w$  block of pixels centered at pixel  $i$  into a column vector  $\mathbf{x}_i$ , which we treat as the feature vector for the vertex  $v_i$ . The Mahalanobis distance  $\rho_{ij}$  between the features  $\mathbf{x}_i, \mathbf{x}_j$  of vertices  $v_i, v_j$  is, see [15]

$$\rho_{ij} = \sqrt{(\mathbf{x}_i - \mathbf{x}_j)^T \Sigma_{i,j}^{-1} (\mathbf{x}_i - \mathbf{x}_j)} \quad (1)$$

where  $\Sigma_{i,j}$  is the covariance matrix between  $\mathbf{x}_i$  and  $\mathbf{x}_j$ . When the distance  $\rho_{ij}$  is below a predetermined threshold  $\tau_\rho$ , the vertices  $v_i, v_j$  are connected by an edge; otherwise, they are disconnected. Fig. 2(b) shows the final graph representation of the  $4 \times 4$  image example using both geographical neighbors and feature similarities.

In graph theory, we usually consider *weighted* graphs [8]. Since not all connected pairs of vertices have the same distances, we capture this fact by using a weight function on the edges. We adopt a Gaussian kernel, suggested by Belkin and Niyogi [10] and used also by Coifman *et al.* [11], to compute the weights  $W_{ij}$  on edges  $e_{ij}$  connecting vertices  $v_i$  and  $v_j$

$$W_{ij} = \begin{cases} \exp\left(-\frac{\rho_{ij}^2}{\sigma^2}\right), & \text{if there is edge } e_{ij} \\ 0, & \text{if no edge } e_{ij} \end{cases} \quad (2)$$

where  $\sigma$  is the Gaussian kernel parameter. The larger  $\sigma$  is, the more weight far away vertices will exert on the weighted graph. The weight  $W_{ij}$  is large when the features of two linked vertices  $v_i, v_j$  are similar.

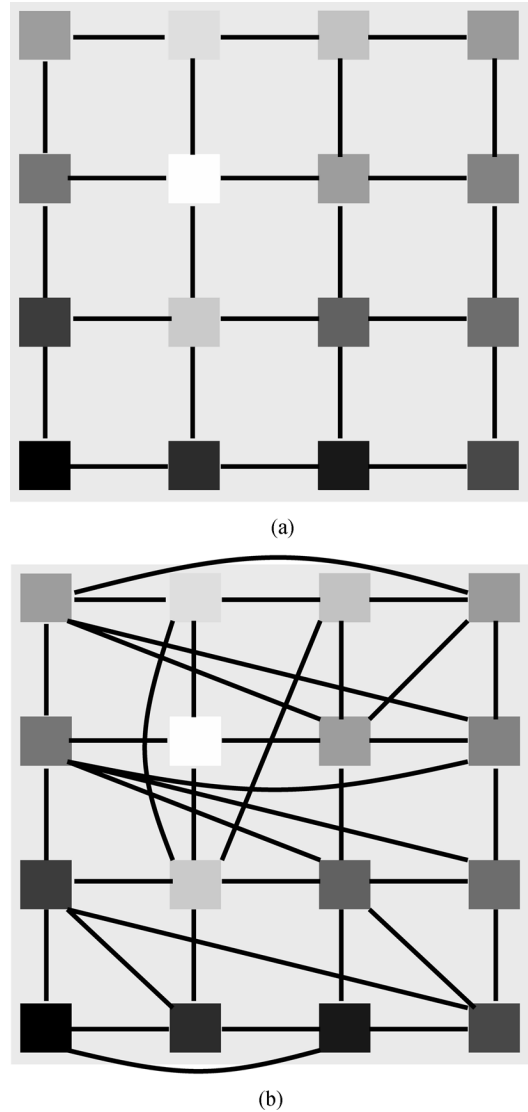


Fig. 2. Illustration of the graph representation of a  $4 \times 4$  image. (a) Edge assignment according to the geographical neighbors. (b) Graph representation using both geographical neighbors and feature similarities.

The weighted graph is equivalently represented by its  $N_{\text{myo}} \times N_{\text{myo}}$  *weighted adjacency matrix*  $\mathbf{W}$  whose elements  $W_{ij}$  are the edge weights in (2). Note that the matrix  $\mathbf{W}$  has a zero diagonal because we do not allow the vertices to be self-connected; it is symmetric since  $W_{ij} = W_{ji}$ .

**B. Graph Partitioning and the Cheeger Constant**

Classification is to partition the set of pixels into disjoint sets. In graph terms, we divide the graph  $G(V, E)$  into two subgraphs. The task is to find out a subset  $E_0$  of edges, called an *edge cut* such that removing this cut separates the graph  $G(V, E)$  into two disconnected subgraphs  $G_1 = (V_1, E_1)$  and  $G_2 = (V_2, E_2)$ , where  $V = V_1 \cup V_2, \emptyset = V_1 \cap V_2$ , and  $E = E_0 \cup E_1 \cup E_2$ . Taking the example of the  $4 \times 4$  image again, the dotted edges shown in Fig. 3(a) assemble an edge cut for the graph. The removal of this edge cut partitions the graph into two parts, as shown in Fig. 3(b).

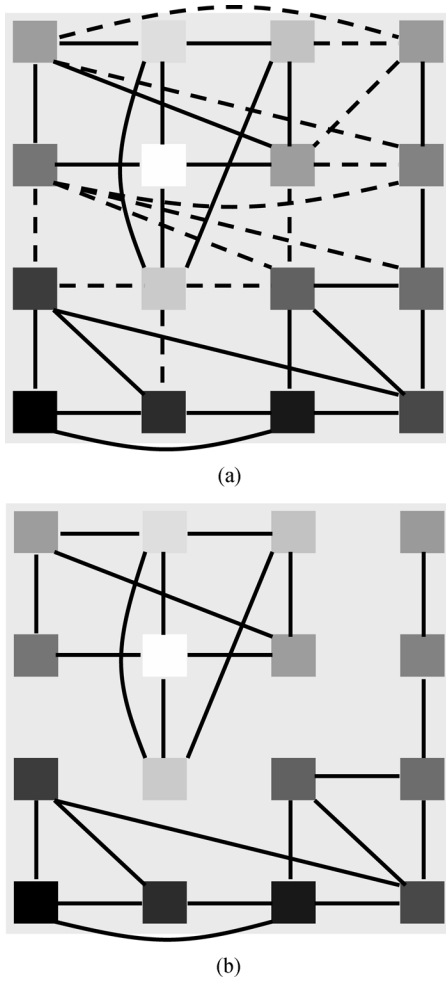


Fig. 3. Conceptualization of an edge cut associated to the  $4 \times 4$  image in Fig. 2(b). (a) Dotted edges assemble an edge cut. (b) Removal of the edge cut partitions the graph.

In the framework of spectral graph theory [8], we define an *optimal* edge cut by looking for the Cheeger constant  $\Gamma(V_1)$  of the graph

$$\Gamma(V_1) = \min_{V_1 \subset V} \frac{|E_0(V_1, V_2)|}{\text{vol}(V_1)} \quad (3)$$

assuming that  $\text{vol}(V_1) \leq \text{vol}(V_2)$ . In (3),  $|E_0(V_1, V_2)|$  is the sum of the edge weights in the cut  $E_0$

$$|E_0(V_1, V_2)| = \sum_{v_i \in V_1, v_j \in V_2} W_{ij}. \quad (4)$$

The volume  $\text{vol}(V_1)$  of  $V_1$  is defined as the sum of the vertex degrees in  $V_1$

$$\text{vol}(V_1) = \sum_{v_i \in V_1} d_i \quad (5)$$

where the degree  $d_i$  of the vertex  $v_i$  is defined as

$$d_i = \sum_{v_j \in V} W_{ij}. \quad (6)$$

To denote the partition of the graph vertices, we introduce an indicator vector  $\chi$  for  $V_1$  whose elements are defined as

$$\chi_i = \begin{cases} 1, & \text{if } v_i \in V_1 \\ 0, & \text{if } v_i \in V_2 \end{cases}. \quad (7)$$

In Appendix A, we derive the Cheeger constant in terms of the indicator vector  $\chi$

$$\Gamma(\chi) = \min_{\chi} \frac{\chi^T \mathbf{L} \chi}{\chi^T \mathbf{d}} \quad (8)$$

where  $\mathbf{L}$  is the graph Laplacian defined in (46) and  $\mathbf{d}$  is the vector collecting vertex degrees. The optimal graph partitioning corresponds to the optimal indicator vector

$$\hat{\chi} = \arg \min_{\chi} \frac{\chi^T \mathbf{L} \chi}{\chi^T \mathbf{d}}. \quad (9)$$

### C. Objective Functional for Cheeger Constant

In (8), the minimization of the cut-to-volume ratio is equivalent to minimizing an objective functional

$$Q(\chi) = \chi^T \mathbf{L} \chi - \beta \chi^T \mathbf{d} \quad (10)$$

where  $\beta$  is the weight. The objective  $Q(\chi)$  is convex, because the graph Laplacian  $\mathbf{L}$  is positive semidefinite, see the Appendix. In addition, the second term  $0 \leq \chi^T \mathbf{d} \leq \text{vol}(V)$  is finite, so the minimizer  $\hat{\chi}$  exists.

Since at each vertex the indicator is either 1 or 0, see (7), there are  $2^{N_{\text{myo}}}$  candidate indicator vectors. When the number of pixels  $N_{\text{myo}}$  in the myocardium is large, it is not computationally feasible to minimize the objective by enumerating all the candidate indicator vectors. The next section proposes a novel algorithm to avoid this combinatorial problem.

## III. OPTIMAL CLASSIFICATION ALGORITHM

This section develops the optimal classifier that utilizes the Cheeger constant.

### A. Spectral Analysis of the Graph Laplacian $\mathbf{L}$

The spectral decomposition of the graph Laplacian  $\mathbf{L}$ , which is defined in (46), gives the eigenvalues  $\{\lambda_n\}_{n=1}^{N_{\text{myo}}}$  and eigenfunctions  $\{\phi^{(n)}\}_{n=1}^{N_{\text{myo}}}$ . By convention, we index the eigenvalues in ascending order. Because the Laplacian  $\mathbf{L}$  is symmetric and positive semidefinite, its spectrum  $\{\lambda_n\}$  is real and nonnegative and its rank is  $N_{\text{myo}} - 1$ . In the framework of spectral graph theory [8], the eigenfunctions  $\{\phi^{(n)}\}$  assemble a complete set and span the Hilbert space of square integrable functions on the graph. Hence, we can express any square integrable function on the graph as a linear combination of the basis functions  $\{\phi^{(n)}\}$ . The domain of the eigenfunctions are vertices, so the eigenfunctions  $\{\phi^{(n)}\}$  are discrete and are represented by vectors. We note that both the eigenfunctions and the vertices are indexed by the set of integers  $I = \{1, 2, \dots, N_{\text{myo}}\}$ . Eigenfunction  $\phi^{(n)}$  is the vector

$$\phi^{(n)} = [\phi_1^{(n)}, \phi_2^{(n)}, \dots, \phi_{N_{\text{myo}}}^{(n)}]^T. \quad (11)$$

We list here the properties of the spectrum of the Laplacian (see [8] for additional details) that will be utilized to develop the classification algorithm.

- 1) For a *connected* graph, there is only one zero eigenvalue  $\lambda_1$ , and the spectrum is

$$0 = \lambda_1 < \lambda_2 \leq \dots \leq \lambda_{N_{\text{myo}}} . \quad (12)$$

The first eigenvector  $\phi^{(1)}$  is constant, i.e.,

$$\phi^{(1)} = \alpha[1, 1, \dots, 1]^T \quad (13)$$

where  $\alpha = 1/\sqrt{N_{\text{myo}}}$  is the normalization factor for  $\phi^{(1)}$ .

- 2) The eigenvectors  $\phi^{(n)}$  with nonzero eigenvalues have zero averages

$$\sum_{i=1}^{N_{\text{myo}}} \phi_i^{(n)} = 0 . \quad (14)$$

The low-order eigenvectors correspond to low-frequency harmonics.

- 3) For a *connected* graph, the Cheeger constant  $\Gamma$  defined by (8) is upper and lower bounded by the following inequality:

$$\frac{1}{2}\lambda_2 \leq \Gamma < \sqrt{2\lambda_2} . \quad (15)$$

Due to the edge assignment strategy of geographical neighborhood, see Section II, our graphs representing the heart images are connected. Therefore, the spectral properties in (12) and (15) hold in our case, besides the property (14) that holds in general.

### B. Expression of Classifier

We now consider the graph  $G(V, E)$  that describes the myocardium in an MRI heart image. The classifier  $\mathbf{c}$  partitioning the graph vertex set  $V$  into two classes  $V_1$  and  $V_2$  is defined as

$$c_i = \begin{cases} 1, & \text{if } v_i \in V_1 \\ -1, & \text{if } v_i \in V_2 \end{cases} . \quad (16)$$

Utilizing the spectral graph analysis, we express the classifier in terms of the eigenbasis  $\{\phi^{(n)}\}$

$$\mathbf{c} = \sum_{n=1}^{N_{\text{myo}}} a_n \phi^{(n)} = \Phi \mathbf{a} \quad (17)$$

where  $a_n$  are the coordinates of the eigen representation,  $\mathbf{a} = [a_1, a_2, \dots, a_{N_{\text{myo}}}]^T$  is a vector stacking the coefficients, and  $\Phi$  is a matrix collecting the eigenbasis

$$\Phi = [\phi^{(1)}, \phi^{(2)}, \dots, \phi^{(N_{\text{myo}})}] . \quad (18)$$

The design of the optimal classifier  $\mathbf{c}$  becomes now the problem of estimating the linear combination coefficients  $a_n$ .

### C. Objective Functional for Classification

In (8), the Cheeger constant is expressed in terms of the set indicator vector  $\chi$  that takes 0 or 1 values. On the other hand, the classifier  $\mathbf{c}$  defined in (16) takes  $\pm 1$  values. We relate  $\chi$  and  $\mathbf{c}$  by the standard Heaviside function  $\mathcal{H}(x)$  defined by

$$\mathcal{H}(x) = \begin{cases} 1, & \text{if } x \geq 0 \\ 0, & \text{if } x < 0 \end{cases} . \quad (19)$$

Hence, the indicator vector  $\chi = [\chi_1, \chi_2, \dots, \chi_{N_{\text{myo}}}]^T$  for the set  $V_1$  is given by

$$\chi_i = \mathcal{H}(c_i) . \quad (20)$$

In (20), the indicator  $\chi$  is a function of the classifier  $\mathbf{c}$  using the Heaviside function  $\mathcal{H}$ . Furthermore, by (17), the classifier  $\mathbf{c}$  is parametrized by the coefficient vector  $\mathbf{a}$ , so the objective functional  $Q$  is parametrized by this vector  $\mathbf{a}$ , i.e.,

$$Q(\mathbf{a}) = \chi(\mathbf{c}(\mathbf{a}))^T \mathbf{L} \chi(\mathbf{c}(\mathbf{a})) - \beta \chi(\mathbf{c}(\mathbf{a}))^T \mathbf{d} . \quad (21)$$

Minimizing  $Q$  with respect to  $\mathbf{a}$  gives the optimal coefficient vector  $\hat{\mathbf{a}}$ , which leads to the optimal classifier  $\mathbf{c} = \Phi \hat{\mathbf{a}}$ . Using eigenbasis to represent the classifier transforms the problem of the combinatorial optimization in (10) to estimating the real-valued coefficient vector  $\mathbf{a}$  in (21).

To avoid estimating too many parameters, we relax the classification function to a smooth function, which simply requires the first  $p$  harmonics in its expression in terms of the eigenbasis. The classifier  $\mathbf{c}$  is now

$$\mathbf{c} = \sum_{n=1}^p a_n \phi^{(n)} = \Phi \mathbf{a} \quad (22)$$

where  $\mathbf{a} = [a_1, a_2, \dots, a_p]^T$  and  $\Phi = [\phi^{(1)}, \phi^{(2)}, \dots, \phi^{(p)}]$ . The estimation of the  $N_{\text{myo}}$  parameters in (17) is reduced to the  $p \ll N_{\text{myo}}$  parameters in (22). As long as  $p$  is chosen small enough, the latter is more numerically tractable than the former.

Another concern in the objective functional (10) is the weighting parameter  $\beta$ . If we knew the Cheeger constant  $\Gamma$ , we could set  $\beta = \Gamma$  and the objective function would be

$$Q(\chi) = \chi^T \mathbf{L} \chi - \Gamma \chi^T \mathbf{d} . \quad (23)$$

The solution would correspond to  $Q(\chi) = 0$ , see (8). However, we cannot set  $\beta = \Gamma$  beforehand, since the Cheeger constant  $\Gamma(\hat{\chi})$  is dependent on the unknown optimal indicator vector  $\hat{\chi}$ .

We can reasonably predetermine  $\beta$  by using one of the spectral properties of the graph Laplacian: The upper and lower bounds of the Cheeger constant are related to the first nonzero eigenvalue  $\lambda_2$  of the graph Laplacian, see (15). The bounds restrain the range of values for the weight  $\beta$ . For simplicity, we set  $\beta$  to the average of the Cheeger constant's upper and lower bounds

$$\beta = \frac{1}{2} \left( \frac{1}{2}\lambda_2 + \sqrt{2\lambda_2} \right) . \quad (24)$$

### D. Minimization Algorithm

Taking the gradient of  $Q(\mathbf{a})$ , we obtain

$$\frac{\partial Q}{\partial \mathbf{a}} = 2 \left( \frac{\partial \chi^T}{\partial \mathbf{a}} \right) \mathbf{L} \chi - \beta \left( \frac{\partial \chi^T}{\partial \mathbf{a}} \right) \mathbf{d} . \quad (25)$$

In (25), the computation of  $(\partial \chi^T / \partial \mathbf{a})$  is

$$\left( \frac{\partial \chi^T}{\partial \mathbf{a}} \right) = \left[ \frac{\partial \chi_1}{\partial \mathbf{a}}, \frac{\partial \chi_2}{\partial \mathbf{a}}, \dots, \frac{\partial \chi_{N_{\text{myo}}}}{\partial \mathbf{a}} \right] \quad (26)$$

$$= \begin{bmatrix} \frac{\partial \chi_1}{\partial a_1} & \frac{\partial \chi_2}{\partial a_1} & \dots & \frac{\partial \chi_{N_{\text{myo}}}}{\partial a_1} \\ \vdots & \vdots & \dots & \vdots \\ \frac{\partial \chi_1}{\partial a_p} & \frac{\partial \chi_2}{\partial a_p} & \dots & \frac{\partial \chi_{N_{\text{myo}}}}{\partial a_p} \end{bmatrix}. \quad (27)$$

Using the chain rule, the entries  $(\partial \chi^T / \partial \mathbf{a})_{mn}$  are

$$\left( \frac{\partial \chi^T}{\partial \mathbf{a}} \right)_{mn} = \frac{\partial \chi_n}{\partial a_m} \quad (28)$$

$$= \frac{\partial \chi_n}{\partial c_n} \frac{\partial c_n}{\partial a_m} \quad (29)$$

$$= \delta(c_n) \frac{\partial \sum_{j=1}^p a_j \phi_n^{(j)}}{\partial a_m} \quad (30)$$

$$= \delta(c_n) \phi_n^{(m)}. \quad (31)$$

In (30),  $\delta(x)$  is the delta (generalized) function defined as the derivative of the Heaviside function  $\mathcal{H}(x)$ .

To facilitate numerical implementation, we use the regularized Heaviside function  $\mathcal{H}_\epsilon$  and the regularized delta function  $\delta_\epsilon$ ; they are defined, respectively, as

$$\mathcal{H}_\epsilon(x) = \frac{1}{2} \left[ 1 + \frac{2}{\pi} \arctan \left( \frac{x}{\epsilon} \right) \right] \quad (32)$$

and

$$\delta_\epsilon(x) = \frac{d\mathcal{H}_\epsilon(x)}{dx} = \frac{1}{\pi} \left( \frac{\epsilon}{\epsilon^2 + x^2} \right). \quad (33)$$

Replaced with the regularized delta function, the explicit expression of  $(\partial \chi^T / \partial \mathbf{a})$  is

$$\left( \frac{\partial \chi^T}{\partial \mathbf{a}} \right) = \begin{bmatrix} \delta_\epsilon(c_1) \phi_1^{(1)} & \delta_\epsilon(c_2) \phi_2^{(1)} & \dots & \delta_\epsilon(c_{N_{\text{myo}}}) \phi_{N_{\text{myo}}}^{(1)} \\ \vdots & \vdots & \dots & \vdots \\ \delta_\epsilon(c_1) \phi_1^{(p)} & \delta_\epsilon(c_2) \phi_2^{(p)} & \dots & \delta_\epsilon(c_{N_{\text{myo}}}) \phi_{N_{\text{myo}}}^{(p)} \end{bmatrix} = \Phi^T \Delta \quad (34)$$

where we define

$$\Delta = \text{diag}(\delta_\epsilon(c_1), \delta_\epsilon(c_2), \dots, \delta_\epsilon(c_{N_{\text{myo}}})) . \quad (35)$$

Substituting (34) into (25), the gradient of the objective has the compact form

$$\frac{\partial Q}{\partial \mathbf{a}} = 2\Phi^T \Delta \mathbf{L} \chi - \beta \Phi^T \Delta \mathbf{d}. \quad (36)$$

The optimal coefficient vector  $\hat{\mathbf{a}}$  is obtained by looking for  $\partial Q / \partial \mathbf{a} = 0$ . We have to solve the minimization numerically, because the unknown  $\mathbf{a}$  is inside the matrix  $\Delta$  and the vector  $\chi$ . We adopt the gradient descent algorithm to iteratively find the solution  $\hat{\mathbf{a}}$ . The classifier  $\mathbf{c}$  is then determined by

$$\mathbf{c} = \Phi \hat{\mathbf{a}}. \quad (37)$$

The vertices with indicators  $\chi_i = \mathcal{H}(c_i) = 1$  correspond to class  $V_1$  and 0 correspond to class  $V_2$ . To select the desired USPIO-labeled regions, the operator simply chooses one of the two classes.

### E. Algorithm Summary

There are two major algorithms in the classifier development: graph representation and classification. We summarize them in Algorithms 1 and 2, respectively.

---

#### Algorithm 1 The graph representation algorithm

---

- 1: **procedure** GRAPHREP( $f$ )   ▷ Load the image  $f$
  - 2: Segment the left ventricle
  - 3: Index all the myocardial pixels by a set of integers  $I = \{1, \dots, N_{\text{myo}}\}$
  - 4: Initialize  $\mathbf{W}$  as an  $N_{\text{myo}} \times N_{\text{myo}}$  zero matrix
  - 5: **for all**  $i \neq j \in I$  **do**
  - 6: Compute Mahalanobis distance  $\rho_{ij}$  by (1)
  - 7: **if**  $\rho_{ij} < \tau_\rho$  or  $i, j$  are geographical neighbors **then**
  - 8:  $W_{ij} \leftarrow$  Compute edge weight  $W_{ij}$  by (2)
  - 9: **end if**
  - 10: **end for**
  - 11: **return**  $\mathbf{W}$
  - 12: **end procedure**
- 

#### Algorithm 2 The classification algorithm

---

- 1: **procedure** CLASSIFIER( $\mathbf{W}$ )
  - 2: Compute graph Laplacian  $\mathbf{L}$  by (46)
  - 3: Eigendecompose  $\mathbf{L}$  to obtain  $\{\lambda_n\}$  and  $\{\phi^{(n)}\}$
  - 4: Compute coefficient  $\beta$  by (24)
  - 5: Initialize classifier coefficient  $\mathbf{a} = \mathbf{1}$  and objective  $Q = \infty$
  - 6: **repeat**
  - 7:  $\mathbf{c} \leftarrow$  Compute classifier  $\mathbf{c}$  by (22)
  - 8:  $\chi \leftarrow$  Compute indicator vector  $\chi$  by (20)
  - 9:  $Q \leftarrow$  Compute objective  $Q$  by (21)
  - 10:  $\mathbf{a} \leftarrow$  Compute  $\mathbf{a} - \partial Q / \partial \mathbf{a}$  by (36)
  - 11: **until**  $\partial Q / \partial \mathbf{a} = 0$
  - 12: **return**  $\chi$
  - 13: **end procedure**
- 

## IV. EXPERIMENTS

This section presents the performance of the classifier with experimentally obtained USPIO-enhanced MRI of phantoms and of transplanted rat hearts. We implement our algorithm with MATLAB on a computer with a 3-GHz CPU and 1 GB RAM. After data acquisition, we normalize the heart image intensities to range from 0 to 1 and manually segment the left ventricle.

1) *Classifier Setting*: There are several parameters needed for running the classifier; their values are described in the following.

- Each vertex  $v_i$  is associated with a  $N_w \times N_w$  block of pixels centered at pixel  $i$  for computing the Mahalanobis distance; see Section II-A. We set  $N_w = 3$ . If  $N_w$  is 1, noise is not taken into account. If  $N_w$  is large, the graph takes better account of the impact of the noise but the computational time for constructing the graph increases. Our choice of  $N_w$  is a compromise between these two issues.
- To derive the image graph, we set  $\sigma = 0.1$  when computing the edge weights in (2). This choice of  $\sigma$  is suggested by Shi and Malik [14], who indicate empirically that  $\sigma$  should be set at 10% of the range of the image intensities.
- The parameter  $\epsilon$  for the regularized Heaviside and delta functions in (32) and (33), respectively, is set to 0.1. The smaller the parameter  $\epsilon$  is, the sharper these two regularized functions are. For  $\epsilon = 0.1$ , the regularized functions are a good approximation to the standard ones.
- To determine the number  $p$  of lowest order eigenfunctions used to represent the classifier  $\mathbf{c}$ , we tested values of  $p$  from 5 to 20. We obtain the best results for  $p = 16$ .
- To reach the minimum of the objective functional, we solve  $\partial Q/\partial \mathbf{a} = 0$  recursively. We stop the iterative process when the norm of the gradient is smaller than  $10^{-4}$  or when the minimization reaches 200 iterations. This number of iterations led to convergence in all of our experiments, although, in most cases, we observed convergence within the first 100 iterations.

A. *Phantom Study*

We design a phantom to investigate how our algorithm performs under various contrast-to-noise ratios (CNRs). The phantom sample consists of three tubes that contain different concentrations of iron-oxide particles and that are surrounded by water. We imaged the phantom with a Bruker AVANCE DRX 4.7-T system with a 5.5-cm home-built surface coil. By adjusting the repetition time (TR), the echo time (TE), or the number of signal averages (NEX), we can generate CNRs from low to high. We run three series of scans.

- Series 1: fixed TR = 1000 ms and NEX = 2; varied TE = 3–15 ms.
- Series 2: fixed TR = 500 ms and TE = 5 ms; varied NEX = 1–12.
- Series 3: fixed TE = 5 ms and NEX = 2; varied TR = 300–1500 ms.

To compute CNR of an image, we begin with calculating signal-to-noise ratios (SNRs) of USPIO-labeled and USPIO-unlabeled regions:

$$\text{SNR}_{\text{lab}} = \frac{\text{average signal of USPIO-labeled regions}}{\text{standard deviation of background noise}} \tag{38}$$

$$\text{SNR}_{\text{unlab}} = \frac{\text{average signal of unlabeled regions}}{\text{standard deviation of background noise}} \tag{39}$$

Then,  $\text{CNR} = |\text{SNR}_{\text{lab}} - \text{SNR}_{\text{unlab}}|$ . The percentage of misclassified pixels is the criterion to evaluate the performance of the classifier. Fig. 4 plots the percentage error versus CNR for

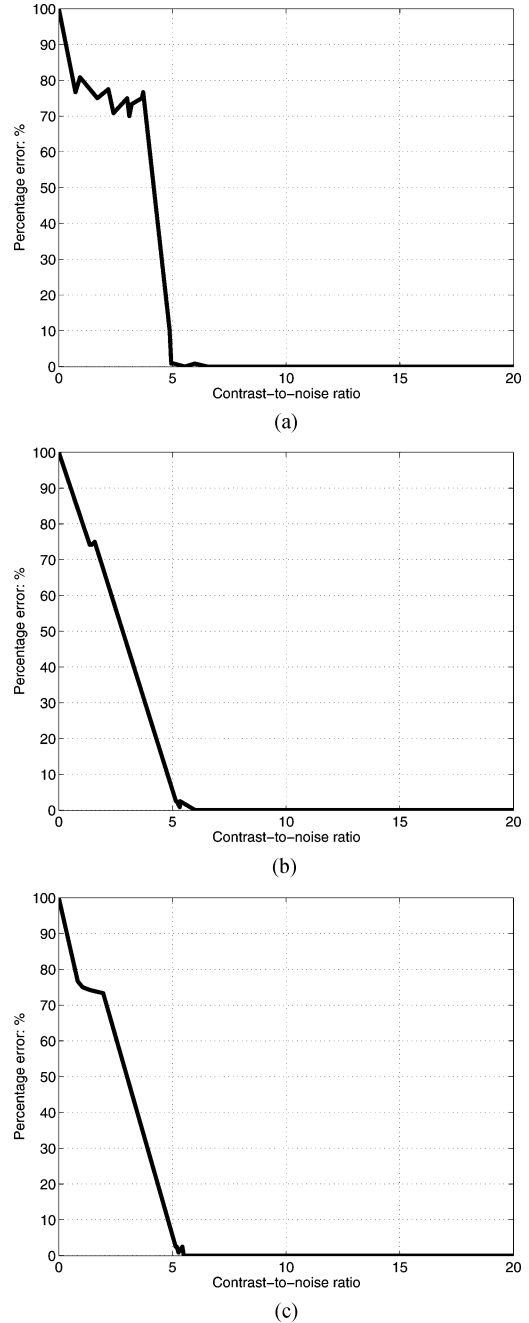


Fig. 4. Percentage error versus CNR on phantom experiments by varying TE, NEX, and TR. (a) Varied TE. (b) Varied NEX. (c) Varied TR.

the three series of scans. With reference to Fig. 4(a)–(c), the proposed algorithm achieves perfect classification when the CNR is larger than 6, but the error increases considerably when the CNR is below 5. This phantom study shows that the classifier can perform without errors when CNR reaches 6 or above.

B. *Cardiac Rejection Study*

1) *USPIO-Enhanced MRI of Heart Transplants*: We have studied the acute cardiac rejection of transplanted hearts using our heterotopic working rat heart model. All rats were male inbred Brown Norway (BN; RT1n) and Dark Agouti (DA; RT1a), obtained from Harlan (Indianapolis, IN), with body weight between 0.18 and 0.23 kg each. We transplanted DA hearts to BN

TABLE I  
SNR AND CNR VERSUS POD

|                                   | POD3  | POD4  | POD5  | POD6  | POD7  |
|-----------------------------------|-------|-------|-------|-------|-------|
| SNR of USPIO-unlabeled myocardium | 24.87 | 20.79 | 16.77 | 25.36 | 21.71 |
| SNR of USPIO-labeled myocardium   | 12.89 | 13.11 | 9.71  | 11.81 | 10.38 |
| CNR of USPIO-enhanced myocardium  | 11.98 | 7.68  | 7.06  | 13.55 | 11.33 |

hosts. Home-made dextran-coated USPIO particles [3] of 27 nm in size were administered intravenously one day prior to MRI with a dosage of 4.5 mg per kg bodyweight.

To investigate the acute cardiac progression, we have imaged five different transplanted rat hearts on postoperation days (PODs) 3, 4, 5, 6, and 7, individually. In our heterotopic rat cardiac transplant model, mild acute rejection begins on POD 3, progresses to moderate rejection on PODs 4 and 5, severe and very severe rejection on PODs 6 and 7, respectively [4]. Each heart was imaged with ten short-axis slices covering the entire left ventricle. *In vivo* imaging was carried out on the same machine in the phantom study.  $T_2^*$ -weighted imaging was acquired with gradient echo recall sequence. Respiratory as well as electrocardiogram gating is used to control respiratory and heart motion artifacts for MR imaging. The MRI protocol has the following parameters: TR = one cardiac cycle (about 180 ms); TE = 8–10 ms; NEX = 4; flip angle = 90°; field-of-view = 3–4 cm; slice thickness = 1–1.5 mm; in-plane resolution = 117–156  $\mu\text{m}$ . The MRI protocol is optimized to guarantee that the classifier works in a valid CNR range. Table I summarizes the SNRs and CNRs in various POD data. The CNRs are all greater than 6, which was the threshold for the classifier to achieve perfect classification in the phantom study.

2) *Automatic Classification Results*: Fig. 5(a) shows different transplanted hearts imaged on PODs 3, 4, 5, 6, and 7. Each image is the sixth slice out of ten acquired short-axis slices for the heart; its location in the heart corresponds to the equator of the left ventricle. Then, we apply our classification algorithm to the images. Fig. 5(b) shows the detected USPIO-labeled areas denoted by red (darker pixels). Unlike time-consuming manual classification, our algorithm takes less than three minutes to localize the regional macrophage accumulation for each image.

To take into account the macrophage accumulation in the 3-D heart, we process multiple slices. Among ten acquired slices, we ignore the first two and the last two slices because they do not clearly contain the myocardium. The classification of rejection on the slices 3–8 determines the volume of myocardial rejection in the 3-D heart.

3) *Validation With Manual Classification*: Wu *et al.* [4] have shown that the dark patches in the MR images are due to those macrophages labeled with USPIO particles whose presence is correlated histologically and immunologically with acute cardiac rejection. Since the best validation option right now is to compare with classification results by a human expert, we treat manually determined USPIO-labeled pixels as the gold standard. In our data set, we can see that manual classification of the heart slices is appropriate for all PODs, except POD5, as we will discuss shortly. Manual classification of all the heart slices at all PODs has been carried out before running the automatic classification. Fig. 5(c) shows the manually classified USPIO-labeled regions. Our automatically detected regions show good

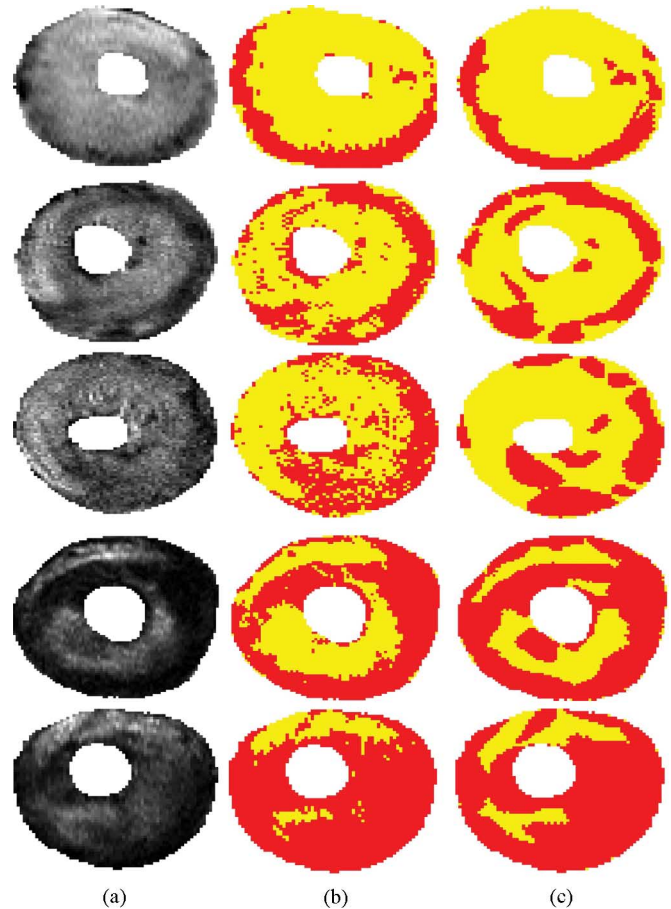


Fig. 5. Application of our algorithm to rejecting heart transplants. Red (darker) regions denote the classified USPIO-labeled pixels. Top to bottom: POD3, POD4, POD5, POD6, and POD7. (a) USPIO-enhanced images. (b) Automatically classified results. (c) Manually classified results.

agreement with the manual results in all slices and PODs, except for POD5. This qualitative validation suggests that our automatic approach is useful in the study of heart rejection based on USPIO-enhanced MRI data.

To quantitatively evaluate the quality of the automatic classification, we have compared the total area of USPIO-labeled regions determined by the classifier and determined manually. In Fig. 6(a), we plot the total macrophage accumulation percentage for slice 6 as a function of the PODs for the data used in Fig. 5. Fig. 6(b) shows similar results but for the whole 3-D heart.

To appreciate better how much the classifier deviates from manual classification, we define the percentage error as

$$P(\varepsilon) = \frac{|\text{Area}_{\text{auto}} - \text{Area}_{\text{manual}}|}{\text{Area}_{\text{myo}}} \quad (40)$$



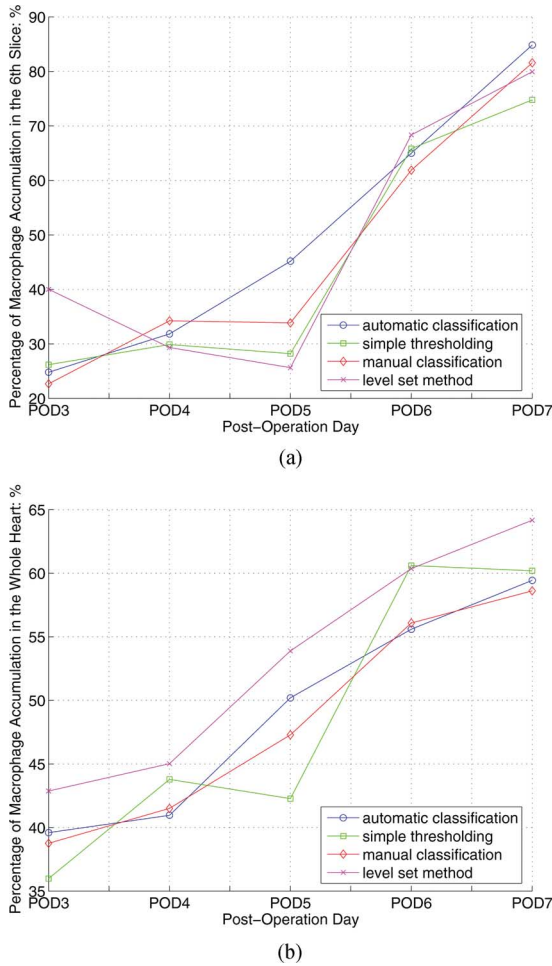


Fig. 6. Immune cell accumulation of the heart transplants in Fig. 5. (a) Slice 6. (b) Whole 3-D heart.

where  $Area_{auto}$  is the USPIO-labeled area by automatic approach,  $Area_{manual}$  the USPIO-labeled area by manual determination, and  $Area_{myo}$  the whole myocardium area. The results are shown in Fig. 7(a). The deviation of the classifier, usually below 4%, shows the very good agreement between the classifier and manual classification for all PODs, except POD5.

We now consider the discrepancy between the automatic classifier and the manual classification results in POD5. The five slices in POD5 heart have percentage errors larger than 6%, with one of them exceeding 10%. POD5 data sets are the most challenging among all POD data sets. This is because POD5 slices are the most noisy, see Table I, and where the macrophages spread dispersively, as rejection spreads from the periphery of the heart (epicardium) to the whole heart. With reference to the POD5 image (middle image) in Fig. 5(a), we see many dark punctate blobs corresponding to the presence of macrophages. Manual selection of these blobs is challenging to a human operator. By missing many of these, the lines displaying the manual classification results (percentage area or percentage volume) in Fig. 6(a) and (b), respectively, fail to be nondecreasing, showing a dip at POD5. Were this true, the level of rejection would have decreased from POD4 to POD5, clearly a contradiction, since the animal models were not treated and rejection becomes more prevalent as time progresses. In contrast, the corresponding plot

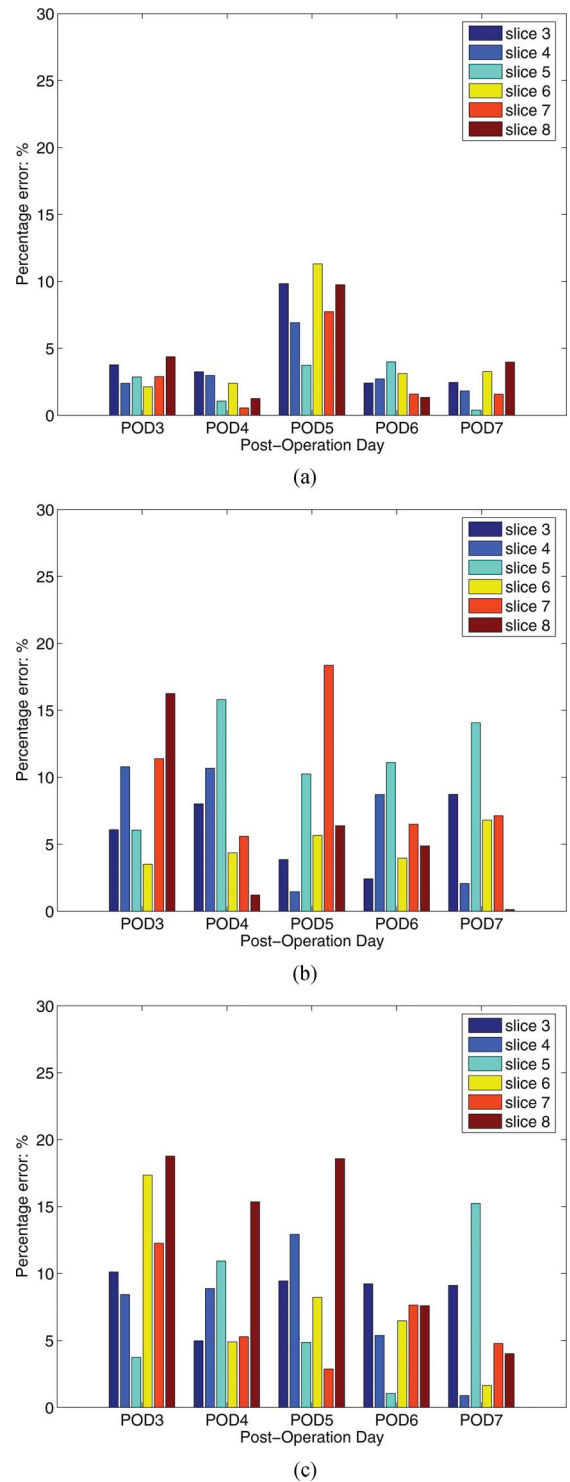


Fig. 7. Percentage deviation of various algorithms versus manual classification results. (a) Automatic classification proposed by this paper. (b) Thresholding method. (c) Level set approach.

lines for the classifier are monotonic—while they track well the manual classification results everywhere else, they deviate from the dip at POD5.

4) *Comparisons With Other Classification Approaches:* In addition to manual classification, simple thresholding is the common automatic method used for classification of USPIO-labeled regions. Fig. 8(a) shows the classification results obtained

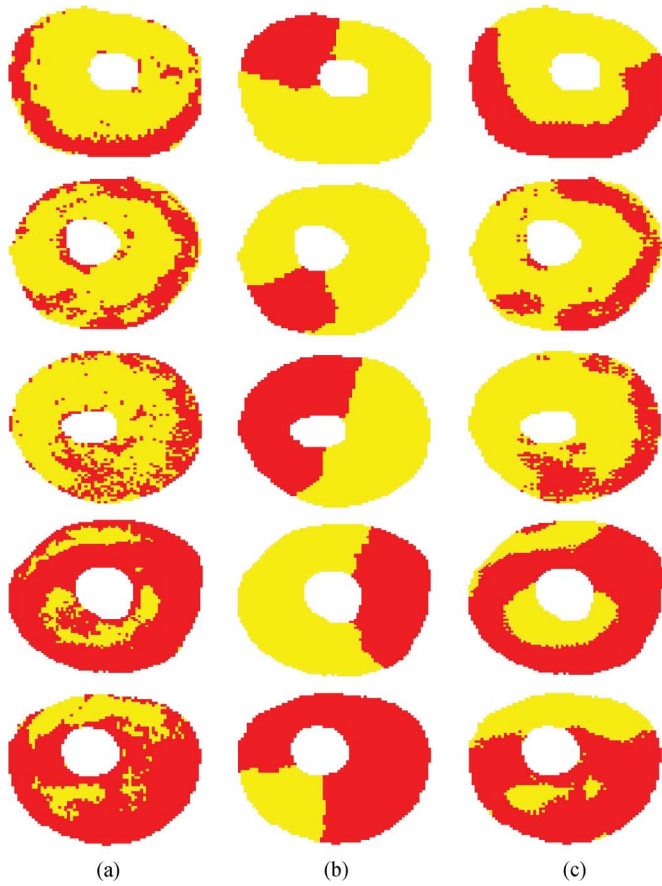


Fig. 8. Application of other algorithms to rejecting heart transplants. Red (darker) regions denote the classified USPIO-labeled pixels. Top to bottom: POD3, POD4, POD5, POD6, and POD7. (a) Thresholding method. (b) Isoperimetric algorithm. (c) Level set approach.

by thresholding the images in Fig. 5(a). Fig. 6(a) and (b) also plot the macrophage accumulation curves using thresholding. The error analysis of the thresholding classification is shown in Fig. 7(b) using the same definition for percentage deviation in (40). Although the classification results by our classifier and by thresholding shown in Fig. 5(b) and Fig. 8(a), respectively, are visually indistinguishable, the quantitative error analysis shown in Fig. 7(b) demonstrates that the thresholding method has higher error rates in most slices than automatic classifier. Further, thresholding is not robust, with error rates that can range from 0.5% to 18.5%, usually with error rates larger than 6%. Thresholding is prone to inconsistency because of the subjectivity in choosing the thresholds and because it does not account for the noise and motion blurring the images.

We provide another comparison by contrasting our algorithm with an alternative classifier, namely, the *isoperimetric partitioning* algorithm proposed by Grady and Schwartz [16]. The isoperimetric algorithm uses also a graph representation, which includes a geographical neighborhood only, not taking into account the noise for edge weights, as in our approach. The isoperimetric algorithm tries to minimize the objective function  $c^T Lc$ , where  $c$  is the real-valued classification function and  $L$  is the graph Laplacian. The minimization is equivalent to solving the linear system  $Lc = 0$ . We applied this method to the images in Fig. 5(a). The classification results are shown in

Fig. 8(b). Comparing these results with the manual classification results in Fig. 5(c), we conclude that the isoperimetric partitioning algorithm fails completely on this data set. The problems with this method are twofold. First, the objective function captures the edge cut but ignores the volume enclosed by the edge cut. This contrasts with our functional, the Cheeger constant, that captures faithfully the goal of minimizing the cut-to-volume ratio. Second, although the desired classifier of the isoperimetric partitioning is a binary function, the actual classifier it considers is a relaxed real-valued function. Our approach addresses this issue via the Heaviside function.

The final comparison is between our proposed method and the *level set* approach [17], [18], which has been applied successfully to segment the heart structures [19]. The level set method finds automatically contours that are the zero level of a level set function defined on the image and that are boundaries between USPIO-labeled and -unlabeled pixels. The optimal level set is obtained to meet the desired requirements: 1) the regions inside and outside the contours have distinct statistical models; 2) the contours capture sharp edges; and 3) the contours are as smooth as possible. Finally, we can classify the pixels enclosed by the optimal contours as USPIO-labeled areas. The experimental results using the level set approach are shown in Fig. 7(c) and Fig. 8(c). In the heart images, macrophages are present not only in large regions but also in small blobs with irregular shapes whose edges do not provide strong forces to attract contours. The contour evolution tends to pass small blobs and capture large continua, leading to more misclassification than our proposed method.

The performance of our proposed classifier may be affected when artifacts are present in the MR images. Our method establishes the graphical representation of the images from geographical and intensity similarities among pixels. If a myocardial region has hypointensity due to artifacts, its intensity features are similar to those of USPIO-labeled pixels and the classifier will have a hard time to distinguish correctly between the artifacts and the USPIO-labeled regions. Although artifacts were not present in our data sets, the operator may need to invoke an artifact removal algorithm before running our classifier.

5) *Future Work*: The classifier presented in this paper performs binary classification of the myocardial pixels and then determines the rejection severity by counting the number of pixels per volume involved in USPIO-labeling. Since macrophage infiltration depends on the rejection severity, less for mild rejection, more for severe rejection, the USPIO-labeled rejecting tissue does not contribute the same levels of MR signals. In future work, we will extend this classifier to handle multiple classes to provide an integrated mechanism to measure rejection severity.

From the results shown in Fig. 5(b), we see that the transplanted hearts have heterogeneous patterns of macrophage infiltration consistent with the histological and immunological findings reported in [4]. The results shown in Fig. 6 are in agreement with the findings that more macrophages are infiltrated to the transplanted hearts as acute rejection progresses, i.e., with increasing number of days after transplantation. To confirm this hypothesis, we will investigate the correlation between the dysfunctional heart motion [20], [21] and macrophage infiltration.

Once this hypothesis is validated, the automatic classification of USPIO-labeled regions has the potential to help determine the severity of heart rejection in clinical studies.

Last, the application of our classifier can be extended to images enhanced by other contrast agents, for example gadolinium or magnetic iron oxide compounds. As long as the agents create positive contrast, we can apply the algorithm to localize the presence of the contrast agents and to monitor other diseases, such as myocardial scar and infarction.

### V. CONCLUSION

This paper develops an automatic algorithm to classify regional macrophage accumulation of allografts imaged by USPIO-enhanced MRI. Automatic classification is desirable. It lightens the manual work of an expert, prevents inconsistencies resulting from different choices of thresholds that usually plague classification by human operators, and, by accounting in its design explicitly for noise, it is robust to noise. The classifier developed in this paper can assist in studying rejection in heart transplants.

We formulate the classification task as a graph partitioning problem. We associate to an MR image a graph where the graph vertices denote pixels and the graph edges connect neighboring and similar pixels. We treat the classifier as a binary function on the graph. The eigendecomposition of the graph Laplacian provides a basis to represent the classifier. The binary classifier is relaxed to a smooth function by linearly combining several low order eigenbasis functions. The optimal classifier is designed to minimize an objective functional derived from the Cheeger constant of the graph. Our experimental results with USPIO-enhanced MRI data of small animals' cardiac allografts undergoing rejection show that the Cheeger graph partitioning based classifier can determine accurately the regions of macrophage infiltration. These experiments show that it presents better performance than other methods like the commonly used thresholding, the isoperimetric algorithm, and a level set based approach.

### APPENDIX

#### EXPRESSION OF THE CHEEGER CONSTANT $\Gamma$ IN TERMS OF THE INDICATOR VECTOR $\chi$

We can rewrite the vertex degree  $d_i$ , see (6), by considering the vertices  $v_j$  in either  $V_1$  or  $V_2$ ; i.e.,

$$d_i = \sum_{v_j \in V_1} W_{ij} + \sum_{v_j \in V_2} W_{ij}. \quad (41)$$

Assuming that the vertex  $v_i$  is in  $V_1$ , the second term in (41) is the contribution of  $v_i$  made to the edge cut  $|E_0(V_1, V_2)|$ . Taking into account all the vertices in  $V_1$ , we have the edge cut

$$|E_0(V_1, V_2)| = \sum_{v_i \in V_1} \sum_{v_j \in V_2} W_{ij} \quad (42)$$

$$= \sum_{v_i \in V_1} \left( d_i - \sum_{v_j \in V_1} W_{ij} \right). \quad (43)$$

To write (43) in a more compact form, we use the indicator vector  $\chi$  for  $V_1$ , defined in (7). It follows that the edge cut (43) is

$$|E_0(V_1, V_2)| = \chi^T \mathbf{D} \chi - \chi^T \mathbf{W} \chi \quad (44)$$

$$= \chi^T \mathbf{L} \chi \quad (45)$$

where  $\mathbf{D} = \text{diag}(d_1, d_2, \dots, d_{N_{\text{myo}}})$  is a diagonal matrix of vertex degrees, and

$$\mathbf{L} = \mathbf{D} - \mathbf{W} \quad (46)$$

is the Laplacian of the graph; see [8]. Because  $\mathbf{D}$  is diagonal and  $\mathbf{W}$  is symmetric,  $\mathbf{L}$  is symmetric. Further,  $\mathbf{L}$  is positive semidefinite since the row sums of  $\mathbf{L}$  are zeros.

Using the indicator vector  $\chi$ , we express the volume  $\text{vol}(V_1)$  as

$$\text{vol}(V_1) = \sum_{v_i \in V_1} d_i = \chi^T \mathbf{d} \quad (47)$$

where  $\mathbf{d}$  is the column vector collecting all the vertex degrees. Replacing (45) and (47) into the Cheeger constant (3), we write the Cheeger constant in terms of the indicator vector  $\chi$

$$\Gamma(\chi) = \min_{\chi} \frac{\chi^T \mathbf{L} \chi}{\chi^T \mathbf{d}}. \quad (48)$$

### REFERENCES

- [1] C. Ho and T. K. Hitchens, "A non-invasive approach to detecting organ rejection by MRI: Monitoring the accumulation of immune cells at the transplanted organ," *Current Pharm. Biotechnol.*, vol. 5, pp. 551–566, Dec. 2004.
- [2] R. Weissleder, G. Elizondo, J. Wittenberg, C. A. Rabito, H. H. Bengel, and L. Josephson, "Ultrasmall superparamagnetic iron oxide: Characterization of a new class of contrast agents for MR imaging," *Radiology*, vol. 175, pp. 489–493, May 1990.
- [3] S. Kanno, Y. L. Wu, P. C. Lee, S. J. Dodd, M. Williams, B. P. Griffith, and C. Ho, "Macrophage accumulation associated with rat cardiac allograft rejection detected by magnetic resonance imaging with ultrasmall superparamagnetic iron oxide particles," *Circulation*, vol. 104, pp. 934–938, Aug. 2001.
- [4] Y. L. Wu, Q. Ye, L. M. Foley, T. K. Hitchens, K. Sato, J. B. Williams, and C. Ho, "in situ labeling of immune cells with iron oxide particles: An approach to detect organ rejection by cellular MRI," *Proc. Natl. Acad. Sci.*, vol. 103, pp. 1852–1857, Feb. 2006.
- [5] M. Hoehn, E. Küstermann, J. Blunk, D. Wiedermann, T. Trapp, S. Wecker, M. Föcking, H. Arnold, J. Hescheler, B. K. Fleischmann, W. Schwandt, and C. Bührle, "Monitoring of implanted stem cell migration in vivo: A highly resolved in vivo magnetic resonance imaging investigation of experimental stroke in rats," *Proc. Natl. Acad. Sci.*, vol. 99, pp. 16267–16272, Dec. 2002.
- [6] R. A. Trivedi, J.-M. U-King-Im, M. J. Graves, J. J. Cross, J. Horsley, M. J. Goddard, J. N. Skepper, G. Quartey, E. Warburton, I. Joubert, L. Wang, P. J. Kirkpatrick, J. Brown, and J. H. Gillard, "In vivo detection of macrophages in human carotid atheroma: Temporal dependence of ultrasmall superparamagnetic particles of iron oxide-enhanced MRI," *Stroke*, vol. 35, pp. 1631–1635, Jul. 2004.
- [7] M. Sirol, V. Fuster, J. J. Badimon, J. T. Fallon, P. R. Moreno, J.-F. Toussaint, and Z. A. Fayad, "Chronic thrombus detection with in vivo magnetic resonance imaging and a fibrin-targeted contrast agent," *Circulation*, vol. 112, pp. 1594–1600, Nov. 2005.
- [8] F. R. K. Chung, *Spectral Graph Theory*, ser. Regional Conference Series in Mathematics. Providence, RI: Amer. Math. Soc., 1997, vol. 92.
- [9] J. Cheeger, "A lower bound for the smallest eigenvalue of the Laplacian," in *Problems in Analysis*, R. C. Gunning, Ed. Princeton, NJ: Princeton Univ. Press, 1970, pp. 195–199.

- [10] M. Belkin and P. Niyogi, "Laplacian eigenmaps for dimensionality reduction and data representation," *Neural Comput.*, vol. 15, pp. 1373–1396, 2003.
- [11] R. R. Coifman, S. Lafon, A. B. Lee, M. Maggioni, B. Nadler, F. Warner, and S. W. Zucker, "Geometric diffusions as a tool for harmonic analysis and structure definition of data: Diffusion maps," *Proc. Natl. Acad. Sci.*, vol. 102, pp. 7426–7431, May 2005.
- [12] D. L. Donoho and C. Grimes, "Hessian eigenmaps: Locally linear embedding techniques for high dimensional data," *Proc. Nat. Acad. Sci.*, vol. 100, no. 10, pp. 5591–5596, May 2003.
- [13] H.-H. Chang, J. M. F. Moura, Y. L. Wu, and C. Ho, "Immune cells detection of *in vivo* rejecting hearts in USPIO-enhanced magnetic resonance imaging," in *Proc. IEEE Int. Conf. Eng. Medicine Biol. Soc.*, New York, Aug. 2006, pp. 1153–1156.
- [14] J. Shi and J. Malik, "Normalized cuts and image segmentation," *IEEE Trans. Pattern Anal. Mach. Intell.*, vol. 22, no. 8, pp. 888–905, Aug. 2000.
- [15] R. O. Duda, P. E. Hart, and D. G. Stork, *Pattern Classification*, 2nd ed. New York: Wiley-Interscience, 2001.
- [16] L. Grady and E. L. Schwartz, "Isoperimetric graph partitioning for image segmentation," *IEEE Trans. Pattern Anal. Mach. Intell.*, vol. 28, pp. 469–475, Mar. 2006.
- [17] S. Osher and J. Sethian, "Fronts propagating with curvature-dependent speed: Algorithms based on Hamilton," *J. Comput. Phys.*, vol. 79, pp. 12–49, 1988.
- [18] J. A. Sethian, *Level Set Methods and Fast Marching Methods*, 2nd ed. Cambridge, U.K.: Cambridge Univ. Press, 1999.
- [19] C. Pluempitwiriyawej, J. M. F. Moura, Y. L. Wu, and C. Ho, "STACS: New active contour scheme for cardiac MR image segmentation," *IEEE Trans. Med. Imag.*, vol. 24, no. 5, pp. 593–603, May 2005.
- [20] H.-H. Chang, J. M. F. Moura, Y. L. Wu, K. Sato, and C. Ho, "Reconstruction of 3-D dense cardiac motion from tagged MR sequences," in *Proc. 2nd IEEE Int. Symp. Biomed. Imag.: Macro Nano*, Arlington, VA, Apr. 2004, pp. 880–883.
- [21] H.-H. Chang, J. M. F. Moura, Y. L. Wu, and C. Ho, "Early detection of rejection in cardiac MRI: A spectral graph approach," in *Proc. 3rd IEEE Int. Symp. Biomed. Imaging: Macro Nano*, Arlington, VA, Apr. 2006, pp. 113–116.